Nano Energy 138 (2025) 110910

Contents lists available at ScienceDirect

Nano Energy

journal homepage: www.elsevier.com/locate/nanoen

Full paper

High-temperature-resistance flexible piezoelectric sensor via cyclized PAN/BTO nanofibers

Tingting Zhou [a], Shenglong Wang [a], Yong Ao [a], Boling Lan [a], Yue Sun [a], Guo Tian [a], Tao Yang [a], Longchao Huang [a], Long Jin [a], Lihua Tang [b], Weiqing Yang [a,c], Weili Deng [a,*]

[a] Key Laboratory of Advanced Technologies of Materials (Ministry of Education), School of Materials Science and Engineering, Southwest Jiaotong University, Chengdu 610031, PR China
[b] Department of Mechanical and Mechatronics Engineering, University of Auckland, Auckland 1010, New Zealand
[c] Research Institute of Frontier Science, Southwest Jiaotong University, Chengdu, Sichuan 610031, PR China

ARTICLE INFO

Keywords:
Piezoelectric nanofibers
High-temperature stability
Mechanical vibration monitoring
Cyclized PAN
Flame retardancy

ABSTRACT

Maintaining stable sensing performance in extreme environments, such as high temperatures, is critical for accurate signal monitoring. Conventional rigid sensors fail to fit on uneven surfaces and polymer-based piezoelectric sensors degrade at elevated temperatures, restricting their utilization in harsh environments. Herein, we design a flexible and high-temperature-resistant piezoelectric sensor based on cyclized polyacrylonitrile (PAN) and barium titanate (BTO) nanoparticles. Computational and experimental results indicate that the integration of BTO into the PAN matrix increases the interfacial dipole interactions and raises the activation energy of the PAN cyclization reaction (E_a = 221.63 kJ/mol). As a result, the developed sensor exhibits a broad operating temperature range (room temp. to 500 °C), an improved piezoelectric performance (d_{33} = 41.5 pC/N), a remarkable frequency response (500 Hz), and an excellent flame-retardant property (*LOI* = 40 %). Supported by machine learning algorithms, the PAN/BTO fiber-based monitoring system achieves accurate fault diagnosis in high-temperature mechanical vibration scenarios, with an impressive accuracy of 96 %. This innovative approach paves the way for designing unique high-temperature-resistant materials and flexible piezoelectric sensors for real-time sensing under harsh conditions.

1. Introduction

Many next-generation energy, transportation, and defense applications require robust and reliable vibration monitoring under extreme environments [1–5], such as automobile engines (100–350 °C) [6–8], aerospace turbomachinery (75–500 °C) [9–11], and petroleum extraction (150–300 °C) [12,13]. For practical applications, sensors capable of maintaining optimal performance at elevated temperatures are essential for ensuring the long-term stability of equipment, preventing failures, and enabling continuous real-time monitoring. In particular, flexible sensors provide a novel solution through conformal attachment to rigid and complex surfaces, thereby substantially improving signal quality [14–18]. Conventional rigid sensors, while effective in some scenarios, are limited in their applications to shape-changing objects or over large-area non-flat surfaces due to their bulkiness and mechanical rigidity [19–21]. In addition, the rigid sensors usually exhibit limited strain tolerance, restricting their use in deformable systems [16,20]. To address these challenges, flexible sensors have emerged as a promising solution, particularly for non-destructive testing and continuous monitoring of small-sized components and curved structures. Especially, nanofiber-based sensors exhibit excellent flexibility, decent sensitivity, and good mechanical durability, providing important insights for developing advanced sensors [22–27]. However, most fiber-based sensors often experience performance degradation with increasing temperatures and even fail beyond critical thresholds, largely due to the thermal instability of the polymers [28–31]. Therefore, there is an urgent need for conformal sensors capable of stable operation in high-temperature regimes.

Rapid advancements in materials science enable the emergence of innovative sensing materials with high mechanical flexibility for high-temperature applications. Ceramics [32–35], semiconductors [36–38] and single crystals [39,40] are often integrated with organic matrices to improve flexibility, yet the resulting composites typically exhibit limited thermal tolerance. Moreover, capacitive or piezoresistive pressure

* Corresponding author.
E-mail address: weili1812@swjtu.edu.cn (W. Deng).

https://doi.org/10.1016/j.nanoen.2025.110910
Received 6 December 2024; Received in revised form 19 March 2025; Accepted 21 March 2025
Available online 24 March 2025

sensors based on these materials tend to respond slowly [41–43], which is insufficient for monitoring high-frequency mechanical vibrations. In contrast, polymer-based piezoelectric materials, such as polyvinylidene fluoride (PVDF) and its derivatives, offer greater mechanical flexibility and high-frequency response but suffer from poor thermal stability. For example, PVDF loses its piezoelectricity at temperatures above its Curie point (80 °C) and completely fails at its melting point of 177 °C [44]. To address these limitations, several strategies have been explored, including crosslinking to restrict polymer chain mobility [45], the incorporation of inorganic fillers [46], and hydrogen bond modification [47]. These approaches indeed improve the thermal stability of materials, but there are still challenges in preserving excellent piezoelectricity at high temperatures. Recently, PAN has emerged as a promising candidate, performing potential thermal stability at 550 °C [48] and unexpected piezoelectricity [49,50]. This is mainly due to the fact that each repeating unit of PAN contains a strongly polar cyanide group (—C≡N) with a high dipole moment (4.3 D), imparting notable piezoelectricity [51]. The thermally annealed PAN forms stable aromatic structures, enhancing its high-temperature resilience [52,53]. However, when heated to 500 °C, PAN cyclizes into a structure similar to graphene, dramatically declining piezoelectric performance [48]. Thus, the performance of piezoelectric materials over a wider range of temperatures is still being explored for their application in extreme conditions.

In this work, we improve the thermal degradation threshold of PAN by introducing BTO nanofillers, resulting in a high-temperature-resistant and flexible piezoelectric sensor. The effects of BTO incorporation on the cyclization, thermal stability and piezoelectricity of PAN are revealed through computational simulation and experimental verification, respectively. As a result, the PAN/BTO composite fiber membranes exhibit excellent electromechanical coupling, with an open-circuit voltage (V_{oc}) of 5.2 V, a short-circuit current (I_{sc}) of 144.8 nA under 200 kPa and a piezoelectric coefficient (d_{33}) of 41.5 pC/N. Notably, these nanocomposites maintain stable sensing performance without degradation across a broad temperature range, from room temperature up to 500 °C, and demonstrate durability over 10,000 cycles. As a proof-of-concept, the developed piezoelectric sensors are conformally attached to the curved mechanical structures, demonstrating their excellent performance in high-temperature mechanical vibration monitoring. This strategy represents a significant advancement in developing high-performance piezoelectric materials for next-generation sensors capable of operating in extreme environments, paving the way for large-scale manufacturing and practical implementation of flexible piezoelectric sensors in industries requiring high-temperature environments.

2. Results and discussions

2.1. Design of the high-temperature-resistant piezoelectric sensor

The core of the high-temperature piezoelectric sensor design is the integration of BTO nanoparticles into PAN, which endows the sensor with both flexibility and thermal stability (Fig. 1**a**). The nanofiber consists of a PAN matrix, where the embedded BTO particles enhance piezoelectricity by inducing local polarization in the interfacial region [54]. When heated, the PAN chain undergoes a crucial cyclization reaction, which significantly improves the thermal stability of the material

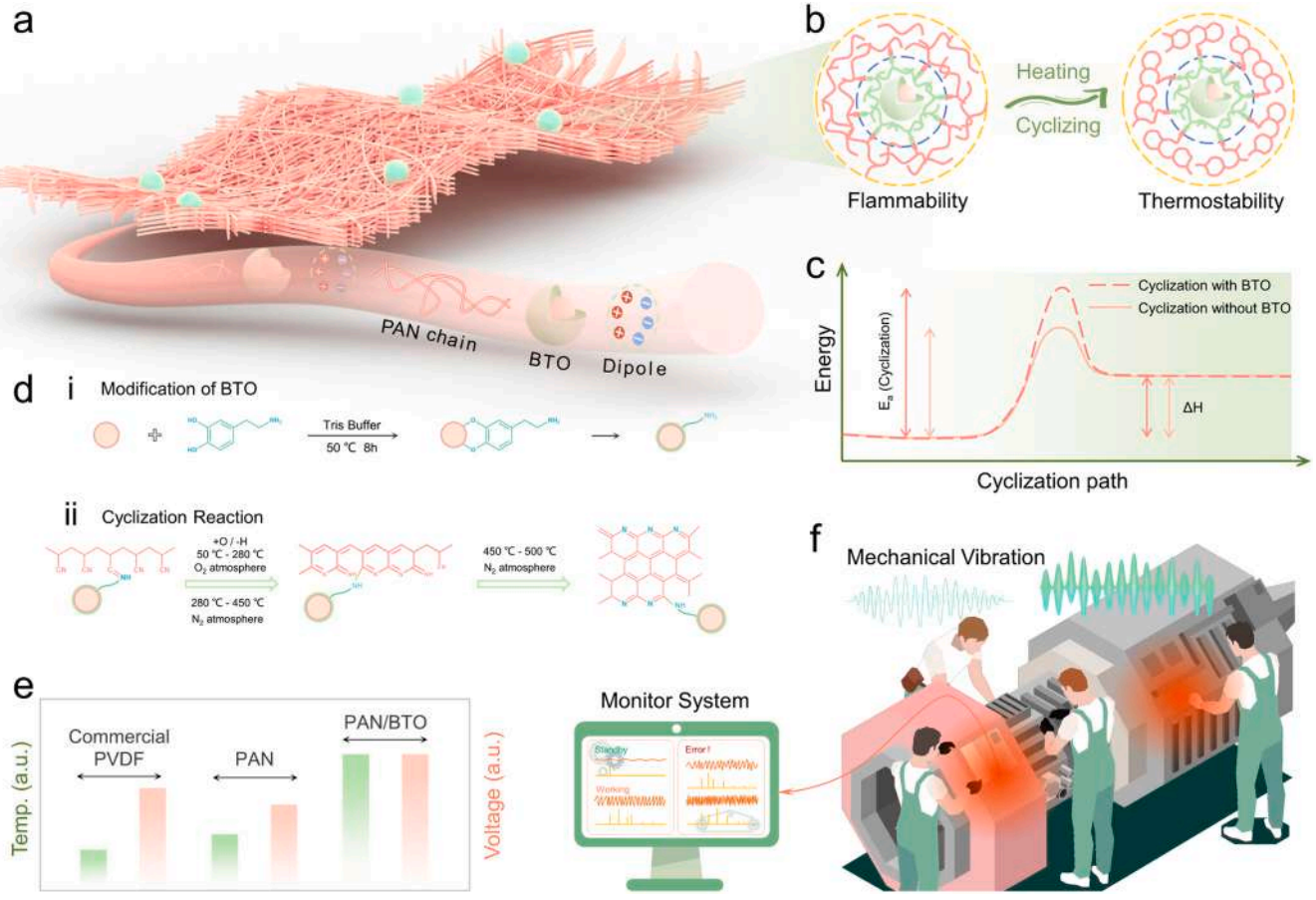

Fig. 1. Overview of high-temperature-resistant PAN/BTO nanofibers. a) Schematic composition of PAN/BTO piezoelectric nanofibers. b) Schematic diagram of the cyclization of PAN/BTO. c) Principle of thermal stability enhancement. BTO increases the apparent reaction activation energy. d) The modification of BTO and the cyclization reaction of PAN/BTO. BTO can inhibit the cyclization reactions. e) Performance comparison of commercial PVDF, pure PAN, and PAN/BTO composites. f) Schematic showing the mechanical vibration monitoring system for real-time vibration sensing and fault diagnosis.

due to the strong bonding of the resulting aromatic network structure (Fig. 1**b**). The inclusion of BTO raises the activation energy required for PAN cyclization, thereby increasing processing temperature (Fig. 1**c**). The elevated activation energy not only enhances flame retardancy but also improves the resistance to degradation at high temperatures. To ensure the uniform distribution of BTO nanoparticles within the PAN matrix, BTO nanoparticles are modified with a poly-dopamine (PDA) coating, reducing surface energy and promoting better dispersion (Fig. 1**d(i)** and Figs. S1–2**)**. For simplicity, the core-shell structure BTO@PDA is subsequently referred to as BTO. In addition, the PAN/BTO

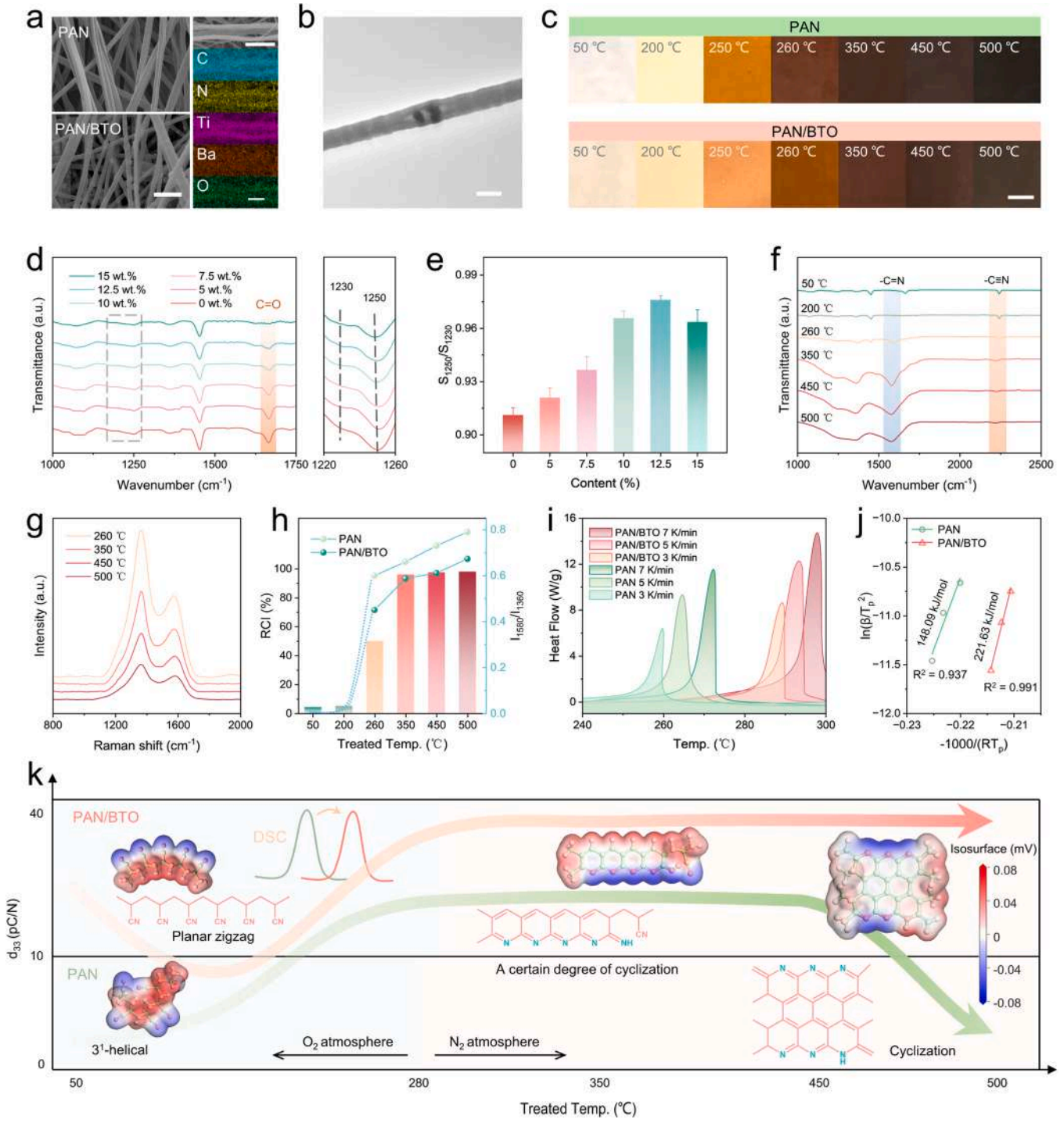

Fig. 2. Characterizations and analysis of PAN/BTO nanofibers. a) SEM images of pure PAN and PAN/BTO nanofibers (Scale bar: 2 μm). The corresponding elemental maps of C, N, Ti, Ba, O (Scale bar: 10 μm). b) TEM image of a single PAN/BTO nanofiber (Scale bar: 500 nm). c) Optical photograph of the PAN and PAN/BTO nanofibers after thermal annealing at various temperatures (50–500 °C). Scale bar: 4 mm. d) FTIR spectra of PAN/BTO nanofibers with different concentrations of BTO from 0 to 15 wt%. e) Calculation of the content of planar zigzag configuration in PAN/BTO nanofibers. S_{1230} and S_{1250} represent the peak areas at 1230 cm^{-1} and 1250 cm^{-1} , respectively. f) FTIR spectra of 12.5 wt% PAN/BTO nanofibers with different thermal annealing from 50 °C to 500 °C. g) Raman spectra of 12.5 wt% PAN/BTO nanofibers with different thermal annealing from 260 °C to 500 °C. h) Relative cyclization index (*RCI*) and degree of graphitization (I_{1580}/I_{1360}) for PAN and PAN/BTO nanofibers treated at different temperatures. i) DSC curves comparing PAN and PAN/BTO nanofibers at different heating rates. j) Arrhenius plot of activation energy for cyclization in PAN and PAN/BTO nanofibers. k) Schematic illustration of the cyclization pathway for PAN and PAN/BTO nanofibers.

nanofibers are thermally annealed at various temperatures ranging from 50 °C to 500 °C (Fig. S3), enhancing the thermal resistance and piezoelectric properties. During the thermal annealing, the PAN chain undergoes oxidation, dehydrogenation, and cyclization, forming an aromatic network structure (—C═N—C═N—), which is essential for high-temperature resilience (Fig. 1**d(ii)**). This behavior contrasts sharply with pure PAN or commercial PVDF, which exhibit performance degradation under comparable thermal conditions (Fig. 1**e** and Fig. S4). The incorporation of BTO nanoparticles, combined with thermal annealing, significantly enhances both the high-temperature resistance and piezoelectric performance of the PAN-based sensor. As a proof-of-concept, a high-temperature real-time vibration monitoring system was designed and validated, including signal acquisition and a neural network model for mechanical fault classification. In which, the detected signals can determine abnormal vibrations and predict possible equipment failures, providing a viable solution for safe equipment operation in high-temperature environments (Fig. 1**f**).

2.2. Fabrication and characterization of the PAN/BTO nanofibers

The well-dispersed PAN/BTO nanofibers are prepared by electrospinning. As illustrated in Fig. 2**a** and Fig. S5-6, BTO nanoparticles with less than 15 % content are homogeneously distributed and well-aligned within the PAN nanofibers. Elemental mapping from Energy Dispersive Spectroscopy (EDS) confirms the even distribution of elements C, Ba, and Ti throughout the composite nanofibers. Transmission Electron Microscopy (TEM) image further reveals the well-dispersed BTO nanoparticles within the PAN nanofiber, displaying a clear and distinct interface between the two materials (Fig. 2**b**). To enhance thermal stability, the PAN/BTO nanofibers undergo a thermal annealing process. During annealing, the color of the resulting fiber membrane changes from light yellow to dark brown, signifying the occurrence of chromophores and an aromatic network structure due to chemical reactions [55]. In contrast, the presence of BTO in the composite is found to delay this color change, indicating that BTO nanoparticles retard the cyclization kinetics of PAN (Fig. 2**c**). The possible reason may be that the introduction of BTO significantly affects the chemical interactions within the composite and the molecular chain configuration of PAN (Fig. 2**d**). Firstly, the strong interfacial interaction between PAN and BTO is evidenced by the reduction in the intensity of the C═O functional group peak (1665 cm^{-1}), indicating the inhibitory effect of BTO on cyclization (Fig. S7). Secondly, the molecular chain configuration of PAN transforms from a 3^1-helix to a planar zigzag conformation, which is known to enhance piezoelectricity [50]. The change in molecular chain conformation is quantified by comparing the ratio of S_{1250} to S_{1230}, where S_{1250} and S_{1230} represent the peak areas at 1230 cm^{-1} and 1250 cm^{-1} in FTIR spectra, corresponding to the conformations of 3^1-helix and planar zigzag, respectively. As can be seen, the proportion of the planar zigzag configuration is maximized when the BTO content reaches 12.5 % (Fig. 2**e**), which also corresponds to the observed optimal V_{oc} and I_{sc} outputs (Fig. S8). Consequently, the PAN/BTO nanofibers with 12.5 wt% BTO are further thermally annealed to explore the behavior at elevated temperatures. As can be seen from the thermogravimetric (TG) test results, the pyrolysis temperature of the PAN/BTO nanofibers material increases with the increase of the thermal annealing temperature (Fig. S9). During thermal annealing, some —C≡N groups are converted to —C═N— groups, forming pyridine structures that benefit thermal stabilization. However, at the same time, more and larger conjugated structures are formed, indicating the graphitization of carbon materials, which is detrimental to the piezoelectric output [55]. The formation of pyridine structures can be quantitatively expressed by the relative cyclization index (*RCI*):

$$RCI = \frac{S_{1580}}{S_{1580} + S_{2240}} \times 100\% \quad (1)$$

where S_{2240} and S_{1580} represent the peak areas at 2240 cm^{-1} and 1580 cm^{-1} in FTIR spectra, corresponding to the stretching vibrations of —C≡N and —C═N— groups, respectively (Fig. 2**f**). The formation of larger conjugated structures can be found in Raman spectroscopy results (Fig. 2**g** and Fig. S10). Typically, the intensity of the 1580 cm^{-1} peak (I_{1580}) represents the graphite crystal structure, while the 1360 cm^{-1} peak (I_{1360}) is associated with disordered structures [56]. As depicted in Fig. 2**h**, the cyclization reaction progresses rapidly before 350 °C, after which it enters a reaction plateau with a relative cyclization degree of more than 90 %, where most of the reactive sites have already transformed, leaving fewer sites for further cyclization. However, the degree of graphitization increases with increasing temperature, negatively impacting the piezoelectric performance due to more ordered, yet less flexible, crystalline structures. Notably, incorporating BTO significantly mitigates the increase of graphitization, thereby preserving the piezoelectricity of the material. Differential scanning calorimetry (DSC) results further validate the beneficial role of BTO in improving the thermal processing of PAN/BTO composites. The DSC curves show a delayed exothermic peak for the cyclization reaction in PAN/BTO nanofiber membranes compared to pure PAN nanofibers, indicating that BTO effectively postpones the cyclization process (Fig. 2**i**). This delay is beneficial in preventing premature cyclization, which in turn reduces the defects in the final carbon nanofibers. The apparent activation energy (E_a) of the cyclization reaction is calculated by the Arrhenius equation:

$$Ln\left(\beta/T_p^2\right) = -\frac{E_a}{R \cdot T_p} + C \quad (2)$$

Where β is the heating rate, T_p is the peak temperature, E_a is the apparent activation energy, R is the gas constant (8.314 J/(mol·K)), C is a constant. The analysis reveals that the E_a of PAN/BTO nanofibers is 221.63 kJ/mol, which is significantly higher than that of pure PAN nanofibers (148.09 kJ/mol), as displayed in Fig. 2**j**. The higher E_a suggests enhanced thermal stability and a slower cyclization rate, reducing the risk of chain breakage and nanofiber melting caused by rapid thermal evolution. Based on these findings, the distinct thermal behaviors of pure PAN and PAN/BTO nanofibers during thermal annealing are illustrated in Fig. 2**k**. Pure PAN starts with a 3^1-helix, exhibiting relatively low piezoelectric properties (d_{33}). As the temperature increases, the pure PAN begins to cyclize and transform into an aromatic network structure, gradually enhancing its piezoelectric performance. However, the structure of PAN becomes stiffer and more ordered due to graphitization above 450 °C, resulting in a significant decrease in piezoelectricity [48]. In contrast, the incorporation of BTO nanoparticles alters the thermal behavior of PAN, delaying the cyclization process and enhancing its thermal stability. Therefore, the d_{33} of PAN/BTO is expected to remain stable at elevated temperatures, as the presence of BTO mitigates the negative effect of graphitization on piezoelectric performance. Additional experiments with PAN@PDA nanofibers without BTO demonstrate that PDA contributes to thermal stability by delaying cyclization (Fig. S11(a)). However, the piezoelectric performance at high temperatures was significantly lower for PAN@PDA compared to PAN/BTO, indicating that the stabilization of piezoelectricity under these conditions is primarily due to the incorporation of BTO nanoparticles (Fig. S11(b)). In addition, surface charge distribution during PAN cyclization was analyzed using surface electrostatic potential simulation. PAN with planar zigzag and a certain degree of cyclization exhibit higher electrostatic potential, implying stronger hydrogen bond energy. This stronger hydrogen bonding enhances the dipole alignment within the material, which promotes charge transfer and polarization under mechanical stress, thus favoring piezoelectricity [57,58].

2.3. Performance of the PAN/BTO nanofibers in high temperature

The high-temperature performances of PAN/BTO nanofibers are

systematically evaluated through electrical, mechanical, and thermal tests to demonstrate their robustness under extreme conditions. To distinguish the piezoelectric response from triboelectric interference, we conducted both forward and reverse connection tests, as previously reported [59]. As shown in Fig. S12, the results of similar waveforms with opposite polarity from different connections confirm that triboelectric interference is negligible. Fig. 3**a-b** and Fig. S13 illustrate the V_{oc}, I_{sc}, and d_{33} of PAN/BTO nanofibers treated from 50 to 500 °C. The results show an initial decline in performance followed by an increase with heating. The decline is attributed to the breakdown of planar configuration, while the subsequent rise results from the formation of a thermally stable aromatic ring structure. When the thermal annealing temperature is 450 °C, V_{oc} and I_{sc} reach the maximum of 5.2 V and 144.8 nA, respectively. The results show a single-peaked V_{oc} response which differs from the bipolar V_{oc} signals reported in previous studies, due to the measurement principle of the high-impedance electrometer [49,55]. Using an electrometer to measure the charge, d_{33} is calculated to be a staggering 41.5 pC/N (Fig. S14). Compared to pure PAN annealed at 450 °C, the addition of BTO increases the piezoelectric output by about 23.8 %, as shown in Fig. S15. Next, we test the V_{oc} of PAN/BTO nanofibers with different thermal annealing temperatures at different test temperatures (Fig. 3**c** and Fig. S16). The V_{oc} of PAN/BTO nanofibers treated at 450 °C can maintain stable from room temperature to 500 °C, which is a critical requirement for high-temperature applications. A

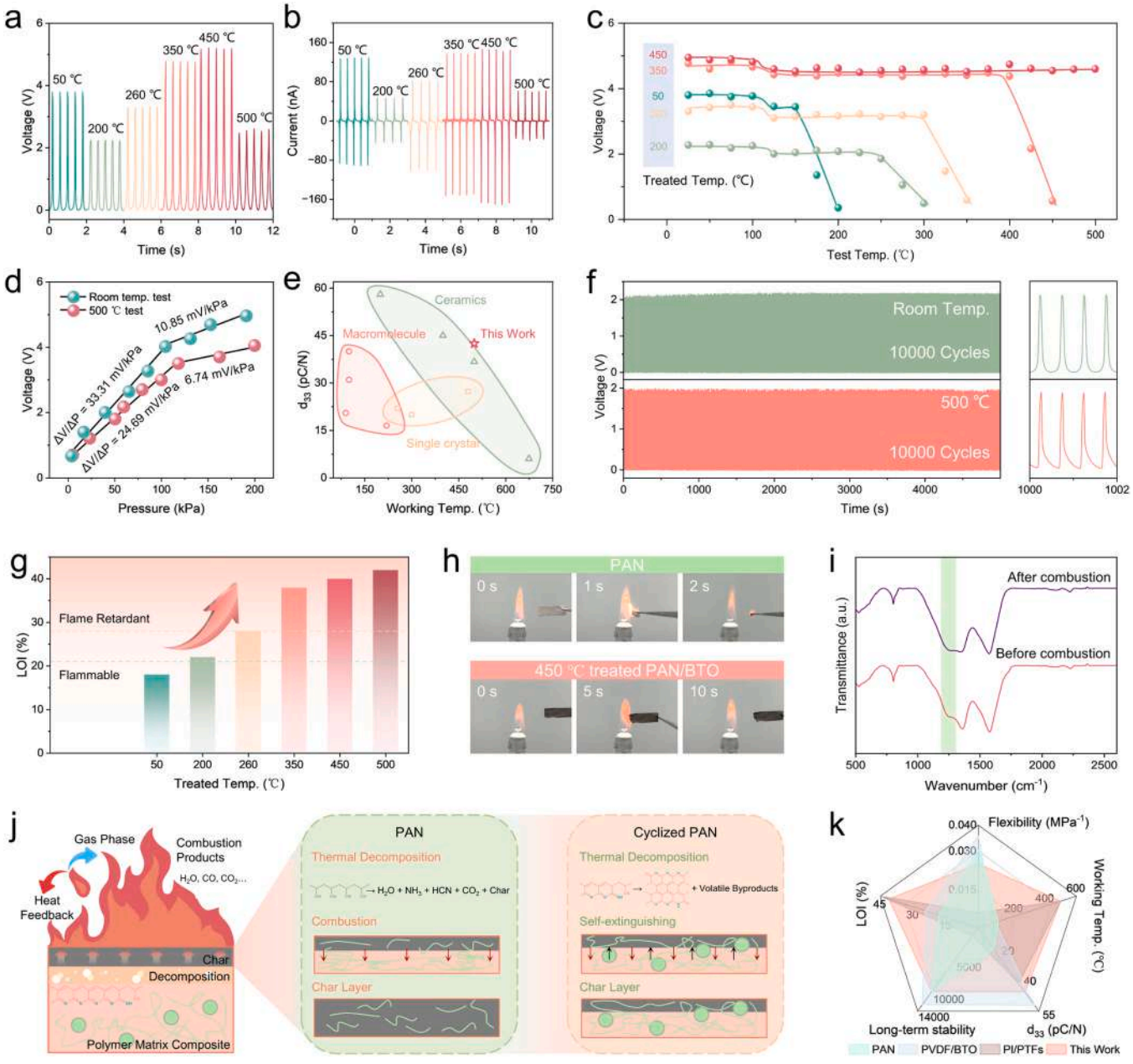

Fig. 3. Sensing performance and flame retardancy of PAN/BTO nanofibers. a) V_{oc} and b) I_{sc} of the 12.5 wt% PAN/BTO nanofibers with different thermal annealing temperatures tested under 200 kPa. c) V_{oc} of 12.5 wt% PAN/BTO nanofibers with different thermal annealing temperatures tested at different temperatures (25 °C to 500 °C) under 200 kPa. d) Sensitivities of PAN/BTO nanofibers treated at 450 °C. e) Comparison of d_{33} in this work with polymers, ceramics and single crystals. f) Long-term stability testing of 450 °C treated PAN/BTO nanofibers under 50 kPa at room temperature and 500 °C. g) *LOI* of PAN/BTO nanofibers treated with different temperatures (50 °C to 500 °C). h) Vertical combustion photographs of PAN and 450 °C treated PAN/BTO nanofibers (2 cm × 6 cm × 130 μm). i) FTIR spectra of 450 °C treated PAN/BTO nanofibers before and after combustion. j) Schematic diagram of the flame-retardant mechanism of PAN/BTO nanofibers. k) Performance comparison of relevant materials in terms of the d_{33}, *LOI*, long-term stability, working temperature and flexibility.

slight decay in V_{oc} is observed at 125 °C, possibly due to the ferroelectric-paraelectric transformation of BTO near Curie temperature, which affects the interfacial polarization, leading to a decrease in the efficiency of charge separation and dipole alignment. To quantify the perception of dynamic mechanical stimuli, the pressure sensitivity is defined as the slope of the output voltage-pressure curve. The PAN/BTO nanofibers thermally annealed at 450 °C show a sensitivity of 33.31 mV/kPa at low pressure (< 100 kPa) and 10.85 mV/kPa in the range of 100–200 kPa, showing good linearity under external forces (Fig. 3**d**). A comparison of PAN/BTO nanofibers with other reported piezoelectric materials (polymers, ceramics and single crystals) [47,48, 60–65] shows superior temperature resistance (up to 500 °C) and piezoelectric performance (41.5 pC/N) due to the internal aromatic ring structure (Fig. 3**e**). Additionally, 10,000 cycles compression/release test were repeated at a pressure of 50 kPa, with virtually no degradation of the output showing the reliable and uniform performance of PAN/BTO nanofibers (Fig. 3**f**).

The flame retardancy and thermal stability of the PAN/BTO nanofibers are assessed using the limiting oxygen index (*LOI*), as shown in Fig. 3**g**. The *LOI* values increase with the treated temperature, indicating enhanced flame retardancy. After treatment at 450 °C, the PAN/BTO nanofibers exhibit a significantly high *LOI* of 40 %, classifying them as flame retardant materials. Vertical combustion tests visually demonstrate PAN/BTO nanofibers' slower burning rate and self-extinguishing properties (Fig. 3**h**). SEM images reveal that pure PAN nanofibers fused into clusters after combustion, while cyclized PAN/BTO nanofibers retain a well-organized structure (Fig. S17). Compared with pure PAN under the same thermal annealing conditions, PAN/BTO nanofibers show similar excellent fire resistance (Fig. S18). FTIR spectra confirm the structure changes of cyclized PAN/BTO nanofibers before and after combustion, supporting the observed thermal stability (Fig. 3**i**). Based on the above research and related structural analysis, the proposed

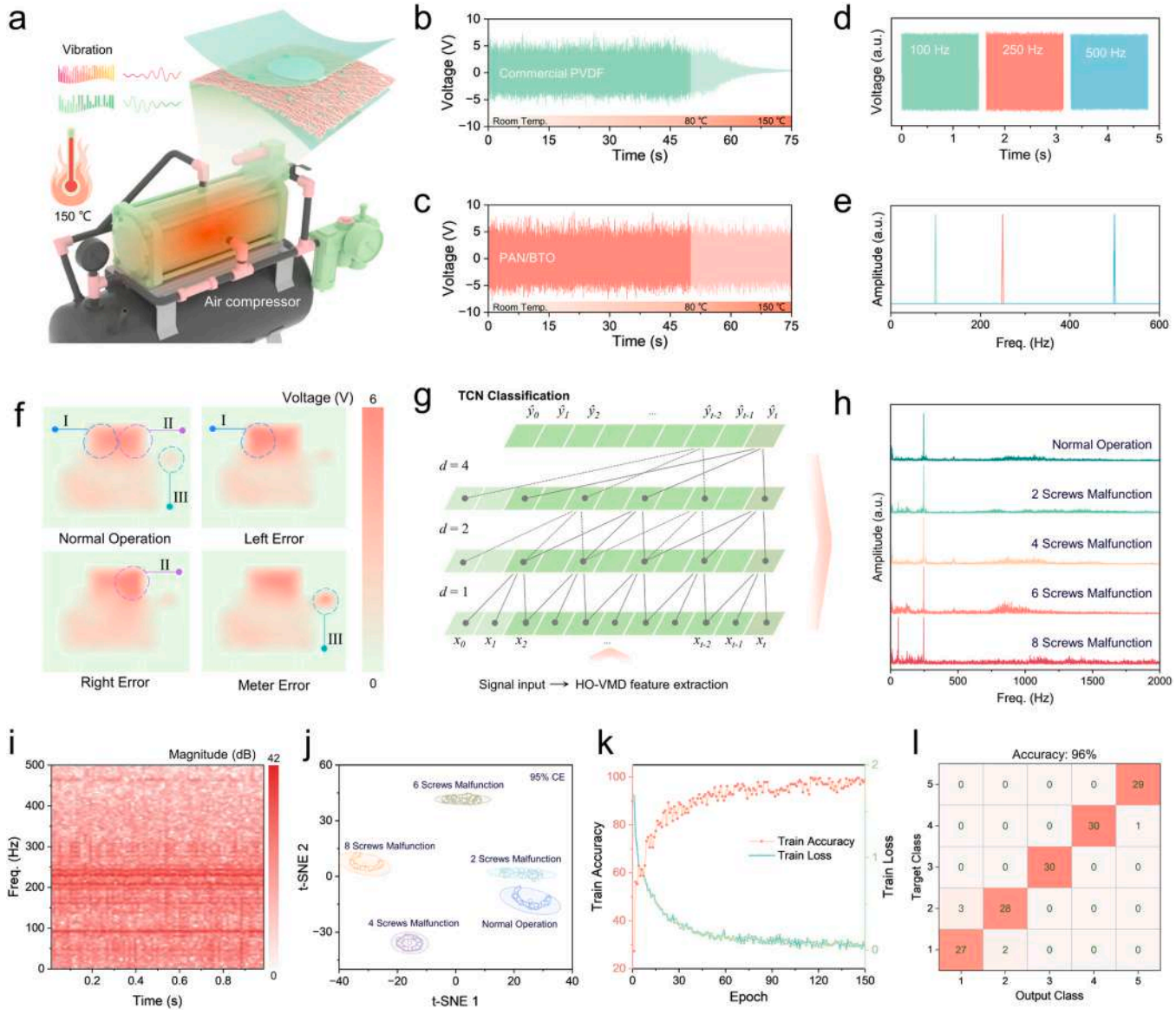

Fig. 4. A deep-learning assisted real-time mechanical vibration monitoring system. a) Schematic illustration of PAN/BTO nanofibers sensor deployed on the air compressor for vibration monitoring. Vibration output of PAN/BTO nanofibers b) and commercial PVDF c) attached to air compressors from room temperature to 150 °C. V_{oc} d) and corresponding FFT e) of PAN/BTO nanofibers sensor under different frequency vibration. f) Heat map of air compressor under different operating conditions. g) Architecture of TCN algorithms. h) FFT spectra of the obtained typical air compressor vibration signals as input to the deep-learning algorithm. i) STFT of eight screws malfunction. j) Visualizing the output data after HO-VMD feature extraction adopting t-SNE dimensionality reduction. k) Classification accuracy and loss function of training datasets in 150 epochs. l) Confusion matrix for test datasets of five vibrations.

flame-retardant mechanism of PAN/BTO nanofibers is shown in Fig. 3**j**. PAN nanofibers undergo complete combustion, resulting in volatile byproducts and the formation of a char layer. In contrast, cyclized PAN demonstrates self-extinguishing behavior due to the formation of a more stable char layer that inhibits further combustion, ensuring safety in high-temperature environments.

Overall, the radar chart highlights the superior long-term stability, working temperatures, *LOI*, d_{33} and mechanical flexibility (the reciprocal of Young's modulus) of the PAN/BTO nanofibers compared to other relevant materials (Fig. 3**k**) [66–68]. This comprehensive assessment demonstrates that PAN/BTO nanofibers not only achieve piezoelectricity comparable to that of high-temperature piezoelectric ceramics but also flexibility rivaling that of polymeric materials, resulting in enhanced safety, reliability, and functionality.

2.4. Machine learning-supervised mechanical vibration monitoring

Mechanical systems in high-temperature environments are particularly vulnerable to failures due to continuous exposure to harsh conditions. Early detection of mechanical faults through vibration monitoring is essential for preventing downtime, reducing maintenance costs, and ensuring operational safety [1,3,4]. As a proof of concept, we demonstrated the developed PAN/BTO nanofibers for monitoring the operating status of an air compressor and determining fault types at high temperatures (Fig. 4**a** and Fig. S19). Conventional flexible sensors (based on commercial PVDF) degrade at elevated temperatures, limiting their applicability in such environments (Fig. 4**b**). In contrast, the developed PAN/BTO piezoelectric sensors demonstrate consistent performance at elevated temperatures up to 150 °C (Fig. 4**c**). This comparison highlights the superior thermal stability and reliability of PAN/BTO sensors for real-time vibration monitoring in extreme environments. Additionally, the dynamic response of the PAN/BTO sensors across a range of frequencies, particularly at 100 Hz, 250 Hz, and 500 Hz, further showcases their reliability in detecting a broad spectrum of vibration signals (Fig. 4**d** and Fig. 4**e**). To provide comprehensive coverage of the compressor's vibration behavior, 15 devices are attached to the surface of the air compressor (Fig. S20). The heat map of voltage distribution under different operating conditions, such as normal operation and fault states (left error (I), right error (II), and meter error (III)), shows noticeable voltage differences, enabling the early detection of mechanical faults (Fig. 4**f**). This real-time monitoring ability is further enhanced through the integration of PAN/BTO sensors with machine learning algorithms, providing a robust solution for fault diagnosis in high-temperature environments. PAN/BTO sensors capture vibration signals from the air compressor, which are analyzed using a Temporal Convolutional Network (TCN) (Fig. 4**g** and Fig. S21). The TCN processes sequential data with dilation factors (*d*) that expand the receptive field, allowing for more comprehensive temporal pattern recognition [69]. Moreover, due to the high performance of PAN/BTO sensors in the frequency domain, the distinct spectral characteristics can be well represented and different operating states can be distinguished (Fig. 4**h**). Typically, the short-time Fourier transform (STFT) further reveals temporal variations in frequency amplitudes (Fig. 4**i**), which can be used to validate the sensor's ability to detect and differentiate operational states. However, the conventional t-SNE analysis, which uses frequency-dependent amplitude as input features for fault classification, does not yield satisfactory results (Fig. S22). To enhance classification accuracy, the Hippo Optimization (HO) algorithm is applied to optimize the Variational Mode Decomposition (VMD) parameters [70]. After feature dimensionality reduction via t-SNE, the five working states become clearly distinguishable as separate clusters, either as normal states or as different screw malfunctions. (Fig. 4**j**). The training accuracy and loss progression indicate steady model convergence after approximately 150 epochs (Fig. 4**k**). The confusion matrix demonstrates that the model accurately classifies all normal operations and faults with a high accuracy of 96 % (Fig. 4**l** and Fig. S23). To highlight the sensor's ability to perform at elevated temperatures, we wear adiabatic gloves to press on a 200 °C heating table, demonstrating its potential for high-temperature applications (**Supplementary Video 1**). Overall, these findings confirm the effectiveness of PAN/BTO piezoelectric nanofibers for intelligent mechanical vibration monitoring and fault diagnosis. The system offers a reliable and scalable solution for industrial applications, even in high-temperature environments, ensuring both accuracy and durability.

Supplementary material related to this article can be found online at doi:10.1016/j.nanoen.2025.110910.

3. Conclusion

In this work, we develop a high-temperature-resistant piezoelectric sensor based on cyclized PAN/BTO nanofibers, offering enhanced thermal stability and excellent vibration monitoring capabilities. Benefiting from the incorporation of BTO and the optimized molecular chain configuration of cyclized PAN, the developed sensors exhibit consistent piezoelectric performance (d_{33} = 41.5 pC/N) up to 500 °C, along with superior flame-retardant properties (*LOI* = 40 %). Furthermore, the sensors demonstrate excellent frequency response, successfully identifying various malfunction scenarios in real time. The integration of this sensor into a machine learning-based diagnostic system allows for precise fault detection and classification with an accuracy of 96 %, even under harsh conditions. This work paves the way for developing advanced piezoelectric sensors with exceptional thermal stability and high sensitivity, showcasing significant potential for electromechanical conversion in high-temperature extreme environments.

4. Experimental section

4.1. Materials

Polyacrylonitrile (PAN, Mw 149000–151000) powders, Nanobarium titanate (BTO, 100 nm), dopamine hydrochloride (DA, 98 %), N,N-dimethylformamide (DMF, 99.9 %) and tris (hydroxymethyl) aminomethane (tris, 99.9 %) were purchased from Aladdin Reagent. In addition, all chemicals were used without further purification.

4.2. Preparation of the PAN/BTO Nanofibers

First, the BTO was subjected to surface modification with DA. The BTO was weighed and dissolved in DMF to obtain solutions with concentrations of 0 wt%, 5 wt%, 7.5 wt%, 10 wt%, 12.5 wt% and 15 wt% relative to the PAN, and co-sonicated for 1 h. Next, PAN powders (11 wt %) were dissolved and stirred in a mixture in water bath at 50 °C for 12 h to form a homogeneous suspension. The mixture was filled into a 10 mL syringe, then the electric field force overcame the surface tension of the droplets on the tip of the needle, forming a Taylor cone that subsequently stretched toward the collector and formed nanofibers. The electrospinning parameters were as follows: the electrospun voltage was 16–18 kV, the inject speed was 1.2 mL/h, and the rotating speed of the grounded roller was controlled at 1200 rpm. The needle-to-collector distance was fixed at 15 cm. The prepared PAN/BTO composite nanofibers were fixed on a high-temperature resistance ceramic plate to prevent shrinkage. Then, PAN/BTO composite nanofibers were placed in a 50 °C oven to evaporate the excess solvent. Finally, oxidation, dehydrogenation and cyclization reactions occurred in the high-temperature tube furnace.

4.3. Fabrication of piezoelectric sensors

Silver electrodes were deposited onto the top and bottom surfaces of the nanocomposite film via magnetron sputtering under an argon atmosphere. After affixing Cu wires using the silver paste, the nanocomposite was encapsulated with a flexible, high-temperature-resistant

polyimide (PI) film. At temperatures reaching 500 °C, the PI film was substituted with a Teflon high-temperature cloth. This encapsulation enhanced device robustness and protected against external influences, such as mechanical stress, temperature fluctuations, and humidity.

4.4. Surface electrostatic potential simulation analysis

Materials Studio software package was used to study the change of surface charge distribution during PAN cyclization. The PAN molecular chain was geometrically optimized using the GGA BLYP function of the DMol3 calculation module. Then, the surface electrostatic potential of the optimized PAN molecular chain was presented by the electron density of the DMol3 analysis module.

4.5. Deep learning for vibration fault classification

The TCN models were developed in MATLAB based on HO and VMD. Firstly, HO algorithm was used to optimize the penalty factors and modal components of VMD. Then, the minimum envelope entropy was used as a fitness function to extract fault characteristics. Finally, the multi-level classification task was completed based on the TCN classification model. The number of convolutional nuclei in the TCN classification model was 16, the size of convolutional nuclei was 3, the number of residual blocks was 2, the initial learning rate was 0.005, the number of training sessions was 150, the learning rate reduction factor was 0.8, and the optimizer was Adam.

4.6. Characterization and measurement

The observation of SEM images and the EDS analysis were characterized by scanning electron microscopy (JSM-7800F, JEOL Ltd.) with an accelerating voltage of 5 kV. The morphology of PAN/BTO nanofibers was obtained by transmission electron microscopy (JEM-2100F, JEOL Ltd.). The XRD (Empyrean, PANalytical), FTIR (Nicolet iS50, ATR) and Raman spectrum (RM2000, 514 nm laser) were applied to study the basic phase and composition of the PAN/BTO composites. The DSC (DSC2500, 25–300 °C, nitrogen atmosphere) and TG (TGA/DSC3 +, 25–800 °C, 10 °C/min, nitrogen atmosphere) were used for thermodynamic behavior analysis. The *LOI* was achieved by a critical oxygen index analyzer (TTech-GBT2406–1) in accordance with the ASTM D2863–97 standard. The size of the sample was 100 × 10 × 0.1 mm^3. To evaluate the pressure sensing performance, a linear motor (LinMot H01–23 × 86/160) equipped with a force probe (M7–50, Mark-10) was employed to apply controlled pressure to the device. A force gauge displayed the pressure in real time, enabling continuous monitoring. The vibration response of the device was precisely controlled using a programmable shaker (Dongling ESS-025) to simulate different operational conditions. The outputs of V_{oc} and I_{sc} were measured using a Keithley 6517 electrometer, providing accurate real-time data for performance evaluation under varying pressure and vibration conditions.

CRediT authorship contribution statement

Deng Weili: Writing – review & editing, Supervision, Funding acquisition, Conceptualization. **Ao Yong:** Writing – review & editing, Resources, Methodology. **Wang Shenglong:** Methodology, Data curation, Conceptualization. **Zhou Tingting:** Writing – original draft, Visualization, Validation, Methodology, Formal analysis, Conceptualization. **Yang Tao:** Writing – review & editing, Resources, Formal analysis. **Tian Guo:** Writing – review & editing, Software, Methodology. **Sun Yue:** Writing – review & editing, Visualization, Investigation. **Lan Boling:** Writing – review & editing, Validation, Data curation. **Yang Weiqing:** Writing – review & editing, Funding acquisition. **Tang Lihua:** Writing – review & editing, Methodology. **Jin Long:** Writing – review & editing. **Huang Longchao:** Writing – review & editing, Software.

Declaration of Competing Interest

The authors declare that they have no known competing financial interests or personal relationships that could have appeared to influence the work reported in this paper.

Acknowledgments

The authors acknowledge the National Natural Science Foundation of China (No. U2330120), the Natural Science Foundation of Sichuan Province of China (No. 2023NSFSC0313), and the Basic Research Cultivation Project of Southwest Jiaotong University (No. 2682023KJ024). The authors also want to thank the full support from the Analysis and Testing Center of Southwest Jiaotong University.

Appendix A. Supporting information

Supplementary data associated with this article can be found in the online version at doi:10.1016/j.nanoen.2025.110910.

Data availability

Data will be made available on request.

References

[1] B. Grocholski, Making vibration sensors noble, Science 353 (2016) 883–884, https://doi.org/10.1126/science.353.6302.883-e.
[2] J.-H. Lee, K.H. Cho, K. Cho, Emerging trends in soft electronics: integrating machine intelligence with soft acoustic/vibration sensors, Adv. Mater. 35 (2023) 2209673, https://doi.org/10.1002/adma.202209673.
[3] Z. Lin, C. Sun, W. Liu, E. Fan, G. Zhang, X. Tan, Z. Shen, J. Qiu, J. Yang, A self-powered and high-frequency vibration sensor with layer-powder-layer structure for structural health monitoring, Nano Energy 90 (2021) 106366, https://doi.org/10.1016/j.nanoen.2021.106366.
[4] I. Mehamud, P. Marklund, M. Björling, Y. Shi, Machine condition monitoring enabled by broad range vibration frequency detecting triboelectric nano-generator (TENG)-based vibration sensors, Nano Energy 98 (2022) 107292, https://doi.org/10.1016/j.nanoen.2022.107292.
[5] Z. Yu, Y. Wan, Y. Qin, Q. jiang, J.-P. Guan, X.-W. Cheng, X. Wang, S. Ouyang, X. Qu, Z. Zhu, J. Wang, H. He, High fire safety thermal protective composite aerogel with efficient thermal insulation and reversible fire warning performance for firefighting clothing, Chem. Eng. J. 477 (2023) 147187, https://doi.org/10.1016/j.cej.2023.147187.
[6] J. Wen, B. Chen, W. Tang, T. Jiang, L. Zhu, L. Xu, J. Chen, J. Shao, K. Han, W. Ma, Z.L. Wang, Harsh-environmental-resistant triboelectric nanogenerator and its applications in autodrive safety warning, Adv. Energy Mater. 8 (2018) 1801898, https://doi.org/10.1002/aenm.201801898.
[7] T. Bhatta, O. Faruk, M.R. Islam, H.S. Kim, S.M.S. Rana, G.B. Pradhan, A. Deo, D.-S. Kwon, I. Yoo, J.Y. Park, Polymeric multilayered planar spring-based hybrid nanogenerator integrated with a self-powered vibration sensor for automotive vehicles IoT applications, Nano Energy 127 (2024) 109793, https://doi.org/10.1016/j.nanoen.2024.109793.
[8] D. Heo, J. Chung, B. Kim, H. Yong, G. Shin, J.-W. Cho, D. Kim, S. Lee, Triboelectric speed bump as a self-powered automobile warning and velocity sensor, Nano Energy 72 (2020) 104719, https://doi.org/10.1016/j.nanoen.2020.104719.
[9] X. Xu, W. Chen, G. Zhao, Y. Li, C. Lu, L. Yang, Wireless whispering-gallery-mode sensor for thermal sensing and aerial mapping, Light Sci. Appl. 7 (2018) 62, https://doi.org/10.1038/s41377-018-0063-4.
[10] A. Ghoshal, J. Ayers, M. Gurvich, M. Urban, N. Bordick, Experimental investigations in embedded sensing of composite components in aerospace vehicles, Compos. Part B-Eng. 71 (2015) 52–62, https://doi.org/10.1016/j.compositesb.2014.10.050.
[11] Y.F. Wang, B. Cao, Y.W. Yang, Y. Yu, P.H. Wang, C.C. Wang, Multi-channel self-powered attitude sensor based on triboelectric nanogenerator and inertia, Nano Energy 107 (2023) 108164, https://doi.org/10.1016/j.nanoen.2022.108164.
[12] X. Lin, M. Salari, L.M.R. Arava, P.M. Ajayan, M.W. Grinstaff, High temperature electrical energy storage: advances, challenges, and frontiers, Chem. Soc. Rev. 45 (2016) 5848–5887, https://doi.org/10.1039/C6CS00012F.
[13] X. Li, L. Zhang, Y. Feng, H. Hu, X. Wang, Y. Zheng, N. Wang, C. Zhang, Q. Yu, F. Zhou, D. Wang, Mechanism and control of triboelectrification on oil-solid interface and self-powered early-warning sensor in petroleum industry, Nano Energy 104 (2022) 107930, https://doi.org/10.1016/j.nanoen.2022.107930.
[14] J. Liu, G. Tian, W. Yang, W. Deng, Recent progress in flexible piezoelectric devices toward human-machine interactions, Soft Sci. 2 (2022) 22.
[15] C. Yang, X. Hou, L. Zhang, Microfluidics-derived microfibers in flexible bioelectronics, Mater. Futures 3 (2024) 032401.

[16] G. Du, Y. Shao, B. Luo, T. Liu, J. Zhao, Y. Qin, J. Wang, S. Zhang, M. Chi, C. Gao, Y. Liu, C. Cai, S. Wang, S. Nie, Compliant iontronic triboelectric gels with phase-locked structure enabled by competitive hydrogen bonding, Nano-Micro Lett. 16 (2024) 170, https://doi.org/10.1007/s40820-024-01387-4.
[17] G. Tian, W. Deng, T. Yang, J. Zhang, T. Xu, D. Xiong, B. Lan, S. Wang, Y. Sun, Y. Ao, L. Huang, Y. Liu, X. Li, L. Jin, W. Yang, Hierarchical piezoelectric composites for noninvasive continuous cardiovascular monitoring, Adv. Mater. 36 (2024) 2313612, https://doi.org/10.1002/adma.202313612.
[18] J. Huang, Y. Cai, G. Xie, X. Xu, Z. Geng, Y. Jiang, Y. Su, Hierarchical carbon nanotube-decorated polyacrylonitrile smart textiles for wearable biomonitoring, Wearable Electron 1 (2024) 180–188, https://doi.org/10.1016/j.wees.2024.07.002.
[19] Z. Wang, Y. Sun, S. Wang, D. Xiong, G. Tian, L. Huang, B. Lan, L. Jin, W. Yang, W. Deng, Insight into piezoelectricity modulation mechanism of ZnO doped with Y ions, J. Mater. Chem. A 12 (2024) 12435–12442, https://doi.org/10.1039/D4TA01317D.
[20] M. Yang, C. Ma, Y. Hu, K. Wang, R. Zhao, Y. Liang, D. Han, H. Wang, R. Zhang, G. Shao, A strain-temperature integrated polymer-derived SiCN ceramic high temperature sensor with wide-range and ultra-short response time, Adv. Funct. Mater. 34 (2024) 2400400, https://doi.org/10.1002/adfm.202400400.
[21] N.-I. Kim, M. Yarali, M. Moradnia, M. Aqib, C.-H. Liao, F. AlQatari, M. Nong, X. Li, J.-H. Ryou, Piezoelectric sensors operating at very high temperatures and in extreme environments made of flexible ultrawide-bandgap single-crystalline AlN thin films, Adv. Funct. Mater. 33 (2023) 2212538, https://doi.org/10.1002/adfm.202212538.
[22] J. Huang, G. Xie, X. Xu, Z. Geng, Y. Su, Degradable multilayer fabric sensor with wide detection range and high linearity, ACS Appl. Mater. Interfaces 16 (2024) 58838–58847, https://doi.org/10.1021/acsami.4c12066.
[23] Q. Jiang, Y. Wan, Y. Qin, X. Qu, M. Zhou, S. Huo, X. Wang, Z. Yu, H. He, Durable and wearable self-powered temperature sensor based on self-healing thermoelectric fiber by coaxial wet spinning strategy for fire safety of firefighting clothing, Adv. Fiber Mater. 6 (2024) 1387–1401, https://doi.org/10.1007/s42765-024-00416-6.
[24] Y. Su, Y. Liu, W. Li, X. Xiao, C. Chen, H. Lu, Z. Yuan, H. Tai, Y. Jiang, J. Zou, G. Xie, J. Chen, Sensing-transducing coupled piezoelectric textiles for self-powered humidity detection and wearable biomonitoring, Mater. Horiz. 10 (2023) 842–851, https://doi.org/10.1039/d2mh01466a.
[25] Y. Su, S. Chen, B. Liu, H. Lu, X. Luo, C. Chen, W. Li, Y. Long, H. Tai, G. Xie, Y. Jiang, Maxwell displacement current induced wireless self-powered gas sensor array, Mater. Today Phys. 30 (2023) 100951, https://doi.org/10.1016/j.mtphys.2022.100951.
[26] C. Chen, G. Xie, J. Dai, W. Li, Y. Cai, J. Li, Q. Zhang, H. Tai, Y. Jiang, Y. Su, Integrated core-shell structured smart textiles for active NO_2 concentration and pressure monitoring, Nano Energy 116 (2023) 108788, https://doi.org/10.1016/j.nanoen.2023.108788.
[27] X. Luo, W. Li, L. Yuan, G. Xie, Y. Su, Self-powered infrared detector enabled by interfacial anchoring and thermal reinforcement, Nano Trends 8 (2024) 100061, https://doi.org/10.1016/j.nwnano.2024.100061.
[28] Y. Zhang, Y. Yu, N. Zhang, T. Zheng, J. Wu, Simultaneous realization of good piezoelectric and strain temperature stability via the synergic contribution from multilayer design and rare earth doping, Adv. Funct. Mater. 33 (2023) 2211439, https://doi.org/10.1002/adfm.202211439.
[29] J. Chen, H. Liu, D. Yu, Q. Li, C. Yuan, J. Xu, S. Cheng, J. Zhao, C. Zhou, G. Rao, Significantly enhancing piezoelectric temperature stability of BNT-based ceramics by constructing the successive ferroelectric-relaxor phase transition, Chem. Eng. J. 480 (2024) 148202, https://doi.org/10.1016/j.cej.2023.148202.
[30] T. Zheng, Y. Yu, H. Lei, F. Li, S. Zhang, J. Zhu, J. Wu, Compositionally graded KNN-based multilayer composite with excellent piezoelectric temperature stability, Adv. Mater. 34 (2022) 2109175, https://doi.org/10.1002/adma.202109175.
[31] R. Yu, X. Wang, W. Wu, C. Pan, Y. Bando, N. Fukata, Y. Hu, W. Peng, Y. Ding, Z. L. Wang, Temperature dependence of the piezophototronic effect in CdS nanowires, Adv. Mater. 25 (2015) 5277–5284, https://doi.org/10.1002/adfm.201501986.
[32] Y. Hong, B. Wang, Z. Long, Z. Zhang, Q. Pan, S. Liu, X. Luo, Z. Yang, Hierarchically interconnected piezoceramic textile with a balanced performance in piezoelectricity, flexibility, toughness, and air permeability, Adv. Funct. Mater. 31 (2021) 2104737, https://doi.org/10.1002/adfm.202104737.
[33] Q. Xu, Y. Tao, Z. Wang, H. Zeng, J. Yang, Y. Li, S. Zhao, P. Tang, J. Zhang, M. Yan, Q. Wang, K. Zhou, D. Zhang, H. Xie, Y. Zhang, C. Bowen, Highly flexible, high-performance, and stretchable piezoelectric sensor based on a hierarchical droplet-shaped ceramics with enhanced damage tolerance, Adv. Mater. 36 (2024) 2311624, https://doi.org/10.1002/adma.202311624.
[34] Q. Xu, Z. Wang, J. Zhong, M. Yan, S. Zhao, J. Gong, K. Feng, J. Zhang, K. Zhou, J. Xie, H. Xie, D. Zhang, Y. Zhang, C. Bowen, Construction of flexible piezoceramic array with ultrahigh piezoelectricity via a hierarchical design strategy, Adv. Funct. Mater. 33 (2023) 2304402, https://doi.org/10.1002/adfm.202304402.
[35] Y. Liu, L. Ding, L. Dai, X. Gao, H. Wu, S. Wang, C. Zhuang, L. Cai, Z. Liu, L. Liu, J. Zhang, Y. Wang, All-ceramic flexible piezoelectric energy harvester, Adv. Funct. Mater. 32 (2022) 2209297, https://doi.org/10.1002/adfm.202209297.
[36] M. Dai, H. Chen, F. Wang, Y. Hu, S. Wei, J. Zhang, Z. Wang, T. Zhai, P. Hu, Robust piezo-phototronic effect in multilayer γ-InSe for high-performance self-powered flexible photodetectors, ACS Nano 13 (2019) 7291–7299, https://doi.org/10.1021/acsnano.9b03278.
[37] M. Li, J. Zheng, X. Wang, R. Yu, Y. Wang, Y. Qiu, X. Cheng, G. Wang, G. Chen, K. Xie, J. Tang, Light-responsive self-strained organic semiconductor for large flexible OFET sensing array, Nat. Commun. 13 (2022) 4912, https://doi.org/10.1038/s41467-022-32647-9.
[38] W. Deng, L. Huang, H. Zhang, G. Tian, S. Wang, T. Yang, D. Xiong, L. Jin, W. Yang, Discrete ZnO p-n homojunction piezoelectric arrays for self-powered human motion monitoring, Nano Energy 124 (2024) 109462, https://doi.org/10.1016/j.nanoen.2024.109462.
[39] P. Marandi, D. Saini, K. Arora, R. Garg, U. Sarkar, K. Parida, D. Mandal, P. P. Neelakandan, Flexible organic molecular single crystal-based triboelectric device as a self-powered tactile sensor, J. Am. Chem. Soc. 146 (2024) 26178–26186, https://doi.org/10.1021/jacs.4c07370.
[40] Y. Liu, Y. Zhang, Z. Yang, H. Ye, J. Feng, Z. Xu, X. Zhang, R. Munir, J. Liu, P. Zuo, Q. Li, M. Hu, L. Meng, K. Wang, D.-M. Smilgies, G. Zhao, H. Xu, Z. Yang, A. Amassian, J. Li, K. Zhao, S. Liu, Multi-inch single-crystalline perovskite membrane for high-detectivity flexible photosensors, Nat. Commun. 9 (2018) 5302, https://doi.org/10.1038/s41467-018-07440-2.
[41] M. Gu, B. Zhao, J. Gao, X. Zhou, L. Huang, J. Wang, L. Wei, C. Yang, M. Chen, Nested-cell architecture and molecular surface modification enabled 10 megapascals range high sensitivity flexible pressure sensors for application in extreme environment, Adv. Funct. Mater. 34 (2024) 2400494, https://doi.org/10.1002/adfm.202400494.
[42] Y. Guo, X. Zhang, F. Jiang, X. Tian, J. Wu, J. Yan, Large-scale synthesis of flexible cermet interdigital electrodes with stable ceramic-metal contact for fire-resistant pressure tactile sensors, Adv. Funct. Mater. 34 (2024) 2313645, https://doi.org/10.1002/adfm.202313645.
[43] L. Wang, M. Zhang, B. Yang, J. Tan, X. Ding, Highly compressible, thermally stable, light-weight, and robust aramid nanofibers/Ti_3AlC_2 MXene composite aerogel for sensitive pressure sensor, ACS Nano 14 (2020) 10633–10647, https://doi.org/10.1021/acsnano.0c04888.
[44] P. Saxena, P. Shukla, A comprehensive review on fundamental properties and applications of poly(vinylidene fluoride) (PVDF), Adv. Compos. Hybrid. Mater. 4 (2021) 8–26, https://doi.org/10.1007/s42114-021-00217-0.
[45] W.E. Kamphunthong, K. Sirisinha, Structure development and viscoelastic properties in silane-crosslinked ethylene–octene copolymer, J. Appl. Polym. 109 (2008) 2347–2353, https://doi.org/10.1002/app.28302.
[46] L. Ren, H. Li, Z. Xie, D. Ai, Y. Zhou, Y. Liu, S. Zhang, L. Yang, X. Zhao, Z. Peng, R. Liao, Q. Wang, High-temperature high-energy-density dielectric polymer nanocomposites utilizing inorganic core–shell nanostructured nanofillers, Adv. Energy Mater. 11 (2021) 2101297, https://doi.org/10.1002/aenm.202101297.
[47] Y.-A. Xiong, S.-S. Duan, H.-H. Hu, J. Yao, Q. Pan, T.-T. Sha, X. Wei, H.-R. Ji, J. Wu, Y.-M. You, Enhancement of phase transition temperature through hydrogen bond modification in molecular ferroelectrics, Nat. Commun. 15 (2024) 4470, https://doi.org/10.1038/s41467-024-48948-0.
[48] W. Wang, Y. Zheng, Y. Sun, X. Jin, J. Niu, M. Cheng, H. Wang, H. Shao, T. Lin, High-temperature piezoelectric conversion using thermally stabilized electrospun polyacrylonitrile membranes, J. Mater. Chem. A 9 (2021) 20395–20404, https://doi.org/10.1039/D1TA04400A.
[49] W. Wang, Y. Zheng, X. Jin, Y. Sun, B. Lu, H. Wang, J. Fang, H. Shao, T. Lin, Unexpectedly high piezoelectricity of electrospun polyacrylonitrile nanofiber membranes, Nano Energy 56 (2019) 588–594, https://doi.org/10.1016/j.nanoen.2018.11.082.
[50] J. Tao, Y. Wang, X. Zheng, C. Zhao, X. Jin, W. Wang, T. Lin, A review: polyacrylonitrile as high-performance piezoelectric materials, Nano Energy 118 (2023) 108987, https://doi.org/10.1016/j.nanoen.2023.108987.
[51] Y. Wang, R. Nakamura, T. Suga, S. Li, Y. Ohki, H. Nishide, K. Oyaizu, Facile synthesis of isotactic polyacrylonitrile via template polymerization in interlayer space for dielectric energy storage, ACS Appl. Polym. 2 (2020) 775–781, https://doi.org/10.1021/acsapm.9b01074.
[52] M. Kopeć, M. Lamson, R. Yuan, C. Tang, M. Kruk, M. Zhong, K. Matyjaszewski, T. Kowalewski, Polyacrylonitrile-derived nanostructured carbon materials, Prog. Polym. Sci. 92 (2019) 89–134, https://doi.org/10.1016/j.progpolymsci.2019.02.003.
[53] F. Yang, W. Liu, M. Yi, L. Ran, Y. Ge, K. Peng, Effect of high temperature treatment on the microstructure and elastoplastic properties of polyacrylonitrile-based carbon fibers, Carbon 158 (2020) 783–794, https://doi.org/10.1016/j.carbon.2019.11.055.
[54] G. Tian, W. Deng, T. Yang, D. Xiong, H. Zhang, B. Lan, L. Deng, B. Zhang, L. Jin, H. Huang, Y. Sun, S. Wang, W. Yang, Insight into interfacial polarization for enhancing piezoelectricity in ferroelectric nanocomposites, Small 19 (2023) 2207947, https://doi.org/10.1002/smll.202207947.
[55] R. Yin, Y. Li, W. Li, F. Gao, X. Chen, T. Li, J. Liang, H. Zhang, H. Gao, P. Li, Y. Zhou, High-temperature flexible electric piezo/pyroelectric bifunctional sensor with excellent output performance based on thermal-cyclized electrospun PAN/$Zn(Ac)_2$ nanofiber mat, Nano Energy 124 (2024) 109488, https://doi.org/10.1016/j.nanoen.2024.109488.
[56] Y.W. Hwang, T.J. Shin, J.H. Seo, M.H. Kim, W.J. Lee, R.S. Ruoff, W.K. Seong, S. H. Lee, Effect of sample geometry on graphitization of polyacrylonitrile, Small 20 (2024) 2400301, https://doi.org/10.1002/smll.202400301.
[57] Z. Han, K. Zhan, X. Wang, G. Zheng, J. Yang, Scalable piezoelectricity in graphene oxide papers tuned by hydrogen bonds, Adv. Electron. Mater. 2 (2016) 1600224, https://doi.org/10.1002/aelm.201600224.
[58] Y. Ren, M. Wu, J.-M. Liu, Ultra-high piezoelectric coefficients and strain-sensitive Curie temperature in hydrogen-bonded systems, Natl. Sci. Rev. 8 (2021) nwaa203, https://doi.org/10.1093/nsr/nwaa203.
[59] C. Chen, S. Zhao, C. Pan, Y. Zi, F. Wang, C. Yang, Z.L. Wang, A method for quantitatively separating the piezoelectric component from the as-received

"Piezoelectric" signal, Nat. Commun. 13 (2022) 1391, https://doi.org/10.1038/s41467-022-29087-w.
[60] K.S. Ramadan, D. Sameoto, S. Evoy, A review of piezoelectric polymers as functional materials for electromechanical transducers, Smart Mater. Struct. 23 (2014) 033001, https://doi.org/10.1088/0964-1726/23/3/033001.
[61] L. Liu, J. Yi, M. Tang, Y. Cui, N.H. Khansur, K.G. Webber, F. Zhu, X. Li, K. Wang, T. Rojac, J. Daniels, D. Damjanovic, S. Wang, Y. Wang, Piezoelectric properties of $BiFeO_3$ exposed to high temperatures, Adv. Funct. Mater. 34 (2024) 2314807, https://doi.org/10.1002/adfm.202314807.
[62] X. Xie, Z. Zhou, R. Liang, X. Dong, Superior piezoelectricity in bismuth titanate-based lead-free high-temperature piezoceramics via domain engineering, Adv. Electron. Mater. 8 (2022) 2101266, https://doi.org/10.1002/aelm.202101266.
[63] J. Haines, O. Cambon, D.A. Keen, M.G. Tucker, M.T. Dove, Structural disorder and loss of piezoelectric properties in α-quartz at high temperature, Appl. Phys. Lett. 81 (2002) 2968–2970, https://doi.org/10.1063/1.1515363.
[64] V.Y. Shur, I.S. Baturin, E.A. Mingaliev, D.V. Zorikhin, A.R. Udalov, E. D. Greshnyakov, Hysteresis-free high-temperature precise bimorph actuators produced by direct bonding of lithium niobate wafers, Appl. Phys. Lett. 106 (2015), https://doi.org/10.1063/1.4907679.
[65] L. Liu, T. Karaki, T. Fujii, Y. Sakai, Effect of substrate material to the properties of screen-printed lead free $(Bi_{0.5}Na_{0.5})TiO_3$-based thick films, Jpn. J. Appl. Phys. 59 (2020) 025502, https://doi.org/10.35848/1347-4065/ab67dd.
[66] Z.-X. Huang, L.-W. Li, Y.-Z. Huang, W.-X. Rao, H.-W. Jiang, J. Wang, H.-H. Zhang, H.-Z. He, J.-P. Qu, Self-poled piezoelectric polymer composites via melt-state energy implantation, Nat. Commun. 15 (2024) 819, https://doi.org/10.1038/s41467-024-45184-4.
[67] S. Yu, J. Milam-Guerrero, Y. Tai, S. Yang, Y.Y. Choi, J. Nam, N.V. Myung, Maximizing polyacrylonitrile nanofiber piezoelectric properties through the optimization of electrospinning and post-thermal treatment processes, ACS Appl. Polym. 4 (2022) 635–644, https://doi.org/10.1021/acsapm.1c01549.
[68] G. Jian, Y. Jiao, Q. Meng, Y. Guo, F. Wang, J. Zhang, C. Wang, K.-S. Moon, C.-P. Wong, Excellent high-temperature piezoelectric energy harvesting properties in flexible polyimide/3D $PbTiO_3$ flower composites, Nano Energy 82 (2021) 105778, https://doi.org/10.1016/j.nanoen.2021.105778.
[69] S. Li, Y.A. Farha, Y. Liu, M.M. Cheng, J. Gall, MS-TCN+ +: Multi-stage temporal convolutional network for action segmentation, IEEE Trans. Pattern Anal. Mach. Intell. 45 (2023) 6647–6658, https://doi.org/10.1109/TPAMI.2020.3021756.
[70] M.H. Amiri, N. Mehrabi Hashjin, M. Montazeri, S. Mirjalili, N. Khodadadi, Hippopotamus optimization algorithm: a novel nature-inspired optimization algorithm, Sci. Rep. 14 (2024) 5032, https://doi.org/10.1038/s41598-024-54910-3.